



**THE INFLUENCE OF SURFACE TEMPERATURE ON AERODYNAMIC HEATING
AND DRAG OF LOW-DENSITY HYPERSONIC WEDGE FLOW**

Wilson F. N. Santos

wilson@lcp.inpe.br

Combustion and Propulsion Laboratory

National Institute for Space Research

Cachoeira Paulista, SP, 12630-000, BRAZIL

***Abstract.** Hypersonic flow past a family of truncated wedges at zero incidence in thermal non-equilibrium is investigated for a range of wall temperature from 440 K to 1760 K. The simulations were performed by using the Direct Simulation Monte Carlo (DSMC) method. The study also focuses the attention of designers of hypersonic configurations on the fundamental parameter of bluntness which can have an impact on even initial design. Some significant differences between sharp and blunt leading edges were noted on the aerodynamic surface quantities such as the heat transfer coefficient, pressure coefficient and total drag. Interesting features observed in the surface fluxes showed that small leading edge thickness compared to the freestream mean free path still has important effects on high Mach number leading edge flows. The analysis is of great importance since it is impossible to achieve ideally sharp leading edges of airframes, such as waveriders.*

Keywords: Hypersonic flow, Rarefied flow, DSMC, Wedge, Aerodynamic heating.

1. INTRODUCTION

Hypersonic waveriders are advanced hypersonic lifting bodies which generate high values of aerodynamic lift-to-drag (L/D) ratio at high Mach numbers. Waverider configurations, introduced by Nonweiler (1959), are derived from a known analytical flowfield, such as flow over a two-dimensional wedge or flow around a slender cone. These configurations are designed analytically with infinitely sharp leading edges for shock wave attachment. Because the shock wave is attached to the leading edge of the vehicle, the upper and lower surfaces of the vehicle can be designed separately. Furthermore, the shock wave acts as a barrier in order to prevent spillage of higher-pressure airflow from the lower side of the vehicle to the upper side, resulting in a high-pressure differential and enhanced lift.

Usually, it is extremely difficult to construct a perfectly sharp leading edge. Any manufacturing error results in a significant deviation from the design contour. Moreover, sharp edges are difficult to maintain because they are easily damaged. Additionally, because heat transfer increases inversely with the nose radius, high heating is associated with sharp edges. Therefore, for practical hypersonic configurations, leading edges should be blunt for heat transfer, manufacturing and handling concerns. Because blunt leading edge promotes shock wave standoff, practical leading edges will have shock detachment, making leading edge blunting a major concern in the design and prediction of flowfields over hypersonic configurations.

The flowfield properties upstream of the leading edge of a body are affected by molecules reflected from the edge region. The degree of the effect is in part conditioned by the edge geometry. In this context, Santos (2002 and 2005) investigated the effect of the frontal-face thickness of truncated wedges on the flowfield structure and on the aerodynamic surface quantities. The thickness effect was examined for a range of Knudsen number, based on the thickness of the frontal face, covering from the transitional flow regime to the free molecular flow one. The emphasis of the works was to provide a critical analysis on maximum allowable geometric bluntness, dictated by either handling or manufacturing requirements, resulting on reduced departures from ideal aerodynamic performance of the vehicle. Thus, allowing the blunted leading edge to more closely represent the original sharp leading edge flowfield. Such analysis is also important when a comparison is to be made between experimental results in the immediate vicinity of the leading edge and the theoretical results, which generally assume a zero-thickness leading edge.

Santos (2003 and 2006) extended further the analysis presented by Santos (2002) on truncated wedges by performing a parametric study on these shapes with emphasis placed on the compressibility effects. The primary goal of the work was to assess the sensitivity of the stagnation point heating, total drag and shock wave standoff distance to changes on the freestream Mach number.

These works (Santos, 2002, 2003, 2005 and 2006) on hypersonic flow past truncated wedges have been concentrated primarily on the analysis of the aerothermodynamic surface quantities by considering the diffuse reflection model as being the gas-surface interaction. However, as a space flight vehicle is exposed to a rarefied environment over a considerable time, a departure from the fully diffuse model is observed, resulting from the colliding molecules that clean the surface of the vehicle, which becomes gradually decontaminated. In this connection, Santos (2004) performed a parametric study on truncated wedges with emphasis placed on the gas-surface interaction effects. In this scenario, the primary interest was to assess the sensitivity of the heat transfer and total drag coefficients to variations on the surface accommodation coefficients experienced by the leading edges.

The current proposed paper extends further the previous analyses on truncated wedges by investigating the impact of the surface temperature on the aerodynamic surface quantities. The

aerodynamic surface quantities on the body surface are affected by molecules reflected from the edge region. The importance of the effect is in part conditioned by the edge geometry as well as by the surface conditions, since the molecules are reflected from the body surface with greater energies with increasing the wall temperature.

In an effort to obtain further insight into the nature of the aerodynamic surface quantities of truncated wedges under hypersonic transitional flow conditions, the primary aim in the present account is to assess the sensitivity of the pressure, skin friction, heat transfer, and drag coefficients to variations on the body-surface temperature.

Under hypersonic transitional flow conditions, at very high speeds and high altitudes, the flow over a given aerodynamic configuration may be sufficiently rarefied that the appropriate molecular mean free path becomes too large, compared to a characteristic length of the vehicle for the use of continuum assumptions but not large enough for the use of the free molecular theory. In such an intermediate or transition rarefied gas regime, where a significant degree of non-equilibrium is observed in the flows, the Direct Simulation Monte Carlo (DSMC) method (Bird, 1994) has been employed in order to solve the problems involving flows of rarefied hypersonic aerothermodynamics.

2. LEADING-EDGE GEOMETRY

The leading-edge geometries are the same as those presented in the previous work (Santos 2005). The truncated wedges are modeled by assuming a sharp-edged wedge of half angle θ with a circular cylinder of radius R inscribed tangent to this sharp leading edge. The truncated wedges are also tangents to the sharp-edged wedge and the cylinder at the same common point. It was assumed a leading edge half angle of 10 degrees, a circular cylinder diameter of 10^{-2} m and frontal-face thickness t/λ_∞ of 0.01, 0.1 and 1, where λ_∞ is the freestream mean free path. Figure 1(a) illustrates schematically this construction. Since the wake region behind the truncated wedges is not of interest in this investigation, it was assumed that the truncated wedges are infinitely long but only the length L is considered.

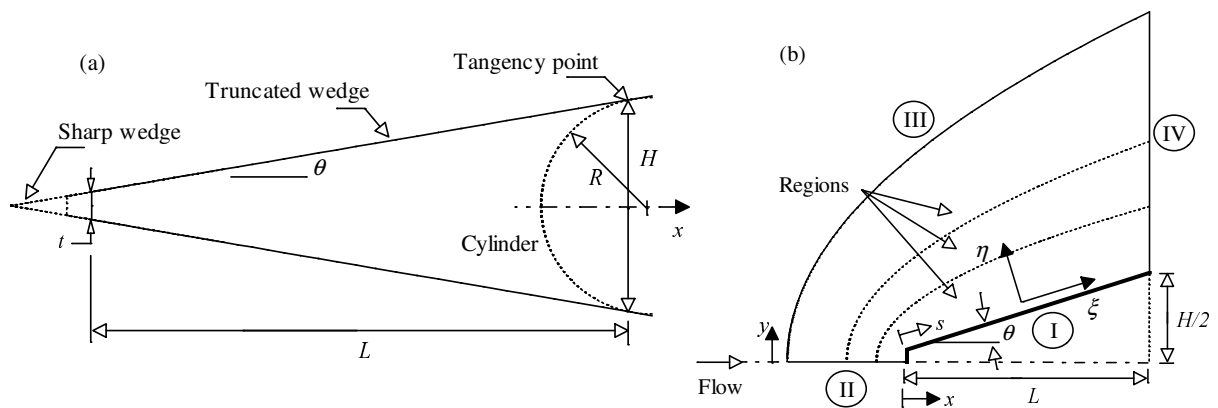


Figure 1: Drawing illustrating (a) the leading edge shapes and (b) the computational domain.

3. COMPUTATIONAL TOOL

The Direct Simulation Monte Carlo (DSMC) method, pioneered by Bird (1994), has become the standard technique for simulating low-density gas dynamics. For these flows, the computational fluid dynamics (CFD) methods that rely on continuum relations to compute the flowfield structure will not provide accurate results in the upper atmosphere, since the

assumptions made in developing the differential equations, on which CFD methods are based, break down on rarefied conditions.

The DSMC method simulates real gas flows with various physical processes by means of a huge number of modeling particles, each of which is a typical representative of great number of real gas molecules. DSMC models the flow as being a collection of discrete particles, each one with a position, velocity and internal energy. The state of particles is stored and modified with time as the particles move, collide, and undergo boundary interactions in simulated physical space. The simulation is always calculated as unsteady flow. However, a steady flow solution is obtained as the large time state of the simulation. Therefore, the DSMC method is basically an explicit time-marching algorithm.

In the present account, collisions are modeled by using the variable hard sphere (VHS) molecular model (Bird, 1981) and the no time counter (NTC) collision sampling technique (Bird, 1989). This model employs the simple hard sphere angular scattering law so that all directions are equally possible for post-collision velocity in the center-of-mass frame of reference. Nevertheless, the collision cross section depends on the relative speed of colliding molecules. The mechanics of the energy exchange processes between kinetic and internal modes for rotation and vibration are controlled by the Borgnakke-Larsen statistical model (Borgnakke and Larsen, 1975). The essential feature of this model is that a part of collisions is treated as completely inelastic, and the remainder of the molecular collisions is regarded as elastic. Simulations are performed using a non-reacting gas model consisting of two chemical species, N_2 and O_2 . Energy exchanges between the translational and internal modes, rotational and vibrational, are considered. Relaxation collision numbers of 5 and 50 were used for the calculations of rotation and vibration, respectively.

4. COMPUTATIONAL FLOW DOMAIN AND GRID

In the DSMC method, the physical space is divided into an arbitrary number of regions, which are subdivided into a certain number of computational cells, and each cell is also divided into subcells. The physical space network is used to facilitate the choice of molecules for collisions and for the sampling of the macroscopic flow properties such as temperature, pressure, density, etc.

In the DSMC algorithm, the linear dimensions of the cells should be small in comparison with the scale length of the macroscopic flow gradients normal to streamwise directions, which means that the cell dimensions should be of the order of or smaller than the local mean free path (Alexander et al., 1998 and 2000). The time step is set such that a typical molecule moves about one third of the cell dimension at each time step. In addition, this time step is much less than the mean collision time (Garcia and Wagner, 2000, and Hadjiconstantinou, 2000), which is defined by the mean time between the successive collisions suffered by any particular molecule.

The computational domain used for the calculation is made large enough so that body disturbances do not reach the upstream and side boundaries, where freestream conditions are specified. A schematic view of the computational domain is depicted in Fig. 1(b). Advantage of the flow symmetry is taken into account, and molecular simulation is applied to one-half of a full configuration.

According to Fig. 1(b), side I is defined by the body surface. Diffuse reflection with complete thermal accommodation is the condition applied to this side. Side II is a plane of symmetry. In such a boundary, all flow gradients normal to the plane are zero. At the molecular level, this plane is equivalent to a specular reflecting boundary. Side III is the freestream side through which simulated molecules enter and exit. Finally, the flow at the

downstream outflow boundary, side IV, is predominantly supersonic and vacuum condition is specified (Guo and Liaw, 2001). At this boundary, simulated molecules can only exit.

Numerical accuracy in DSMC method depends on the grid resolution chosen as well as on the number of particles per computational cell. Both effects were investigated to determine the number of cells and the number of particles required to achieve grid independence solutions. The grid generation scheme used in this study follows that procedure presented by Bird (1994). Along the outer boundary (side III) and the body surface (side I), point distributions are generated in such way that the number of points on each side is the same; ξ -direction in Fig. 1(b). Then, the cell structure is defined by joining the corresponding points on each side by straight lines and then dividing each of these lines into segments which are joined to form the system of quadrilateral cells; η -direction in Fig. 1(b). The distribution can be controlled by a number of different distribution functions that allow the concentration of points in regions where high flow gradients or small mean free paths are expected.

A grid independence study was made with three different structured meshes in each coordinate direction. The effect of altering the cell size in the ξ -direction was investigated with grids of 50(coarse), 100(standard) and 150(fine) cells, and 60 cells in the η -direction for the bluntest leading edge investigated, $t/\lambda_\infty = 1$ case. In analogous fashion, an examination was made in the η -direction with grids of 30(coarse), 60(standard) and 90(fine) cells, and 100 cells in the ξ -direction for the $t/\lambda_\infty = 1$ case. From the total number of cells in the ξ -direction, 30% are located along the frontal surface and 70% distributed along the afterbody surface. In addition, each grid was made up of non-uniform cell spacing in both directions. The effect (not shown) of changing the cell size in both directions on the heat transfer and pressure coefficients was rather insensitive to the range of cell spacing considered, indicating that the standard grid, 100x60 cells, for the $t/\lambda_\infty = 1$ case, is essentially grid independent. A similar procedure in terms of mesh was performed for the other cases investigated.

In a second stage of the grid independence investigation, a similar examination was made for the number of molecules. The standard grid for the $t/\lambda_\infty = 1$ case, 100x60 cells, corresponds to, on average, a total of 190,000 molecules. Two new cases using the same grid were investigated. These two new cases correspond to 104,000 and 283,000 molecules in the entire computational domain. As the three cases presented approximately the same results (not shown) for the heat transfer, pressure and skin friction coefficients, hence the standard grid with a total of 190,000 molecules is considered enough for the computation of the aerodynamic surface quantities. Again, a similar procedure was performed for the other leading-edge thickness cases investigated.

5. COMPUTATIONAL CONDITIONS

The freestream and flow conditions used in the present calculations are those given by Santos (2005) and summarized in Table 1, and the gas properties (Bird, 1994) are shown in Table 2. The freestream velocity V_∞ is assumed to be constant at 3.56 km/s. This velocity corresponds to a freestream Mach number M_∞ of 12. The translational and vibrational temperatures in the freestream are in equilibrium at 220 K.

Table 1. Freestream and flow conditions

Temperature T_∞ (K)	Pressure p_∞ (N/m ²)	Density ρ_∞ (kg/m ³)	Number density n_∞ (m ⁻³)	Viscosity μ_∞ (Ns/m ²)	Mean free path λ_∞ (m)
220.0	5.582	8.753×10^{-5}	1.8209×10^{21}	1.455×10^{-5}	9.03×10^{-4}

Table 2. Gas properties

	Mole fraction X	Molecular mass m (kg)	Molecular diameter d (m)	Viscosity index ω
O ₂	0.237	5.312×10^{-26}	4.01×10^{-10}	0.77
N ₂	0.763	4.650×10^{-26}	4.11×10^{-10}	0.74

The overall Knudsen number Kn is defined as the ratio of the molecular mean free path λ in the freestream gas to a characteristic dimension of the flowfield. In the present study, the characteristic dimension was defined as being the frontal-face thickness t of the truncated leading edges. For the thicknesses investigated, $t/\lambda_\infty = 0.01, 0.1$ and 1 , the overall Knudsen numbers corresponds to $Kn_t = 100, 10$, and 1 . Finally, the Reynolds number Re_t covers the range from 0.193 to 19.3 , based on conditions in the undisturbed stream with frontal-face thickness t as the characteristic length.

In order to simulate the wall temperature effect, the DSMC calculations were performed independently for three distinct numerical values of wall temperature, i.e., T_w of 440 K, 880 K and 1760 K. These values correspond to $2, 4$ and 8 times the freestream temperature, respectively. This temperature range is chosen to be representative of the surface temperature near the stagnation point and is assumed to be uniform over the bodies.

6. COMPUTATIONAL RESULTS AND DISCUSSION

This section focuses on the effects that take place in the aerodynamic surface quantities due to the variations on the wall temperature as well as on the frontal-face thickness of the wedge. Aerodynamic surface quantities of particular interest in the transition flow regime are number flux, heat transfer, pressure, skin friction and drag. In this scenario, this section discusses and compares differences of these quantities expressed in coefficient form.

6.1. Number Flux

As the body surface temperature is increased from 440 to 1760 K, the molecules impinging on the body surface are reflected with greater energies. In this connection, the relative translational velocities of reflected molecules close to the body surface will be increased, thus reducing the net buildup of particle density near the body surface. As a result, changes in the number of molecules colliding with the body surface as well as changes in the incident and reflected momentum and energy of these molecules are expected.

The number flux N is calculated by sampling the molecules impinging on the surface by unit time and unit area. The sensitivity of the dimensionless number flux to variations on the body-surface temperature and on the frontal-face thickness is illustrated in Figs. 2 and 3 for frontal-face thicknesses t/λ_∞ of 0.01 and 1 , that correspond to Kn_t of 100 and 1 , respectively. In this set of figures, the dimensionless number flux N_f stands for the number flux N normalized by $n_\infty V_\infty$, where n_∞ is the freestream number density and V_∞ is the freestream velocity. Also, S is the arc length s along the body surface, measured from the frontal-face/afterbody junction, normalized by the freestream mean free path λ_∞ .

According to these plots, the dimensionless number flux to the surface relies not only on the frontal-face thickness but also on the body-surface temperature. For a sharp leading edge, Kn_t of 100 , the dimensionless number flux is low and constant along the frontal surface and increases gradually along the afterbody surface to a peak value attained around one mean free path downstream the leading-edge shoulder. A similar behavior is seen (not shown) for the slightly blunt leading edge case, Kn_t of 10 . On the other hand, for the bluntest leading edge

case investigated, Kn_t of 1, the dimensionless number flux is large on the frontal surface. It presents almost a constant value in the first half of the frontal face and decreases in the vicinity of the shoulder. After that, it decreases significantly along the afterbody surface. One possible reason for this increase in the dimensionless number flux with increasing the frontal-face thickness may be related to the collisions of two groups of molecules; the molecules reflecting from the body and the molecules oncoming from the freestream. The molecules that are reflected from the body surface, which have a lower kinetic energy interact with the oncoming freestream molecules, which have a higher kinetic energy. Thus, the surface-reflected molecules recollide with the body surface, which produce an increase in the dimensionless number flux in this region. As expected, this behavior is less pronounced with increasing the body-surface temperature, since the molecules are reflected from the surface with greater energies. Consequently, the net buildup of particle density near the body surface is reduced.

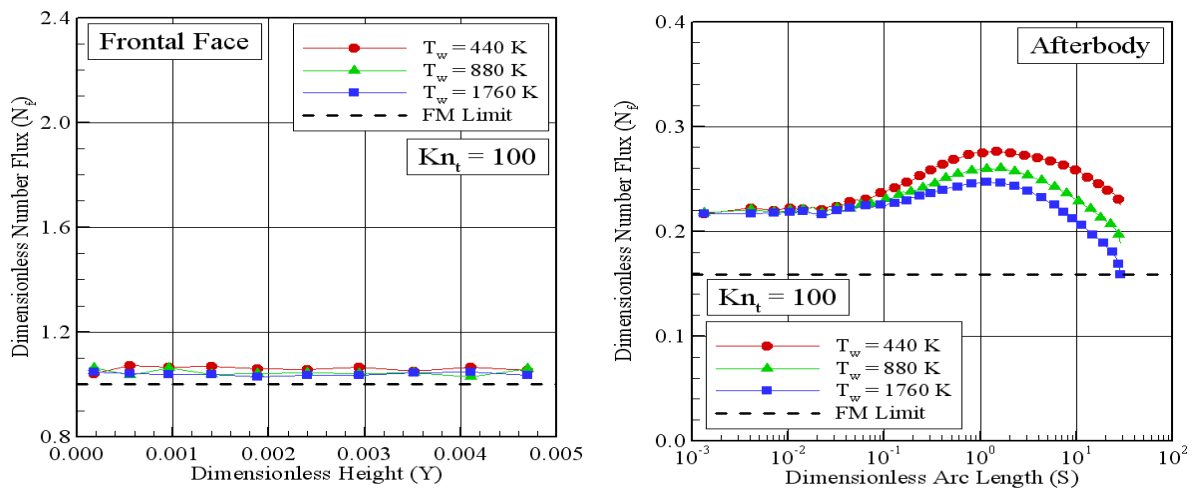


Figure 2: Dimensionless number flux N_f along the (a) frontal face and the (b) afterbody surface as a function of the wall temperature for leading edge corresponding to Knudsen number Kn_t of 100.

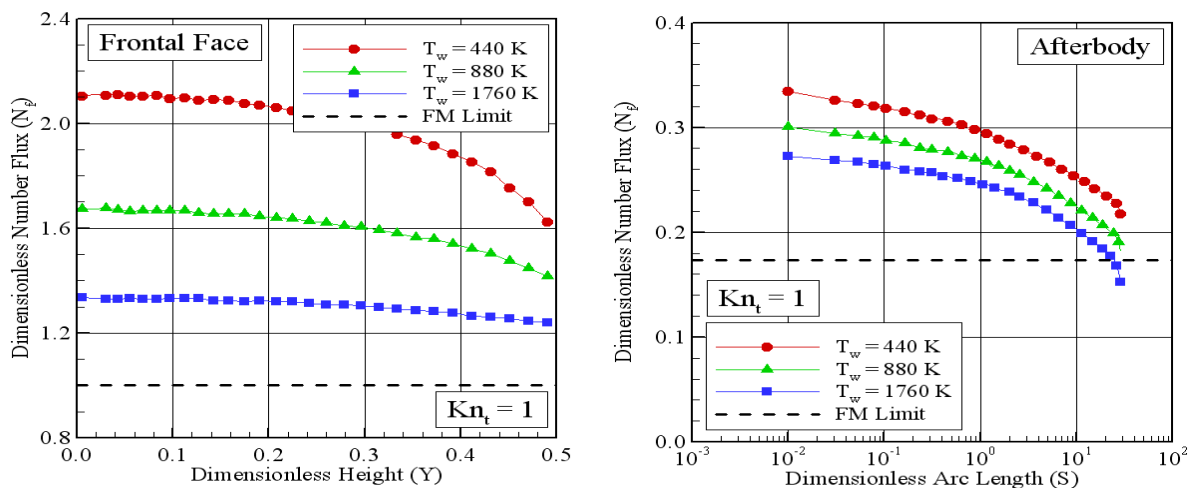


Figure 3: Dimensionless number flux N_f along the (a) frontal face and the (b) afterbody surface as a function of the wall temperature for leading edge corresponding to Knudsen number Kn_t of 1.

For comparison purpose, the dimensionless number flux by considering free molecular flow is also displayed in Figs. 2 and 3. It is seen from Fig. 2(a) that, for the $Kn_t = 100$ case, the dimensionless number flux along the frontal surface approaches the limit value, $N/n_\infty V_\infty = 1$, obtained by the free molecular flow equations (Bird, 1994).

6.2. Heat Transfer Coefficient

The heat transfer coefficient C_h is defined as being,

$$C_h = \frac{q_w}{\frac{1}{2} \rho_\infty V_\infty^3} \quad (1)$$

where q_w is the net heat flux to the body surface and ρ_∞ is the freestream density.

The heat flux q_w to the body surface is calculated by the net energy flux of the molecules impinging on the surface. A flux is regarded as positive if it is directed toward the surface. The net heat flux q_w is related to the sum of the translational, rotational and vibrational energies of both incident and reflected molecules as defined by,

$$q_w = q_i + q_r = \sum_{j=1}^N \left\{ \left[\frac{1}{2} m_j v_j^2 + e_{Rj} + e_{Vj} \right]_i + \left[\frac{1}{2} m_j v_j^2 + e_{Rj} + e_{Vj} \right]_r \right\} \quad (2)$$

where N is the number of molecules colliding with the surface by unit time and unit area, m is the mass of the molecules, v is the velocity of the molecules, e_R and e_V stand for the rotational and vibrational energies, respectively. Subscripts i and r refer to incident and reflected molecules.

Distribution of heat transfer coefficient C_h along the body surface is plotted in Fig. 4 and 5 for Kn_t of 100 and 1, respectively, and parameterized by the wall temperature. It is noticed from Figs. 4 and 5 that the heat transfer coefficient is sensitive to the frontal-face thickness as well as to the body-surface temperature. For a sharp leading edge, Kn_t of 100, the heat transfer coefficient is constant along the frontal-face surface. In contrast, for a blunt leading edge, Kn_t of 1, the heat transfer coefficient remains essentially constant over the first half of the frontal-face surface, but then increases at the vicinity of the frontal-face/afterbody junction. Nevertheless, along the afterbody surface, the heat transfer coefficient presents basically the same behavior for sharp and blunt leading edges in the sense that it decreases downstream along the body surface. As would be expected, the blunter the leading edge is the lower the heat transfer coefficient at the stagnation point. Moreover, the higher the wall temperature the lower the heat transfer coefficient along the frontal-face surface and at the vicinity of the frontal-face/afterbody junction. For purpose of reference, at $T_w = 440$ K, the heat transfer coefficient at the stagnation point for leading edges defined by Kn_t of 100, 10 and 1 corresponds, respectively, to 1.24, 1.26 and 1.30 times the heat transfer coefficient for the same shapes at $T_w = 1760$ K.

Of particular interest is the behavior of the heat transfer coefficient at the vicinity of the frontal-face/afterbody junction. As the number of molecules impinging on the body surface decreases (see Fig. 3) in the vicinity of the leading edge shoulder, then the velocity of the molecules increases in this region in order to increase the heat transfer coefficient in this region. As a matter of fact, a molecular velocity rise in this region is expected due to the flow expansion along the shoulder of the leading edge.

The heat flux to the body surface was defined in terms of the incident and reflected flow properties (see Eq.(2)) and based upon the gas-surface interaction model of fully

accommodated, complete diffuse re-emission. The diffuse model assumes that the molecules are reflected equally in all directions, quite independently of their incident speed and direction. Due to the diffuse reflection model, the reflected velocity of the molecules impinging on the body surface is obtained from a Maxwellian distribution that takes into account for the temperature of the body surface. In this fashion, according to Eq.(2), not only the number of molecules impinging on the surface but also the wall temperature plays a important role on the reflected contribution to the net heat flux to the body surface. In this scenario, it is observed (not shown) that the incident heat flux contributes to increase the heat transfer coefficient along the frontal-face surface of the leading edge. With the wall temperature rise, the buildup of particle density near the body surface is reduced (Santos, 2008), allowing the molecules oncoming from the freestream to transfer more energy to the body surface. Nevertheless, with increasing the wall temperature, the reflected heat flux also increases, and results in lower net heat flux, according to Eq. (2).

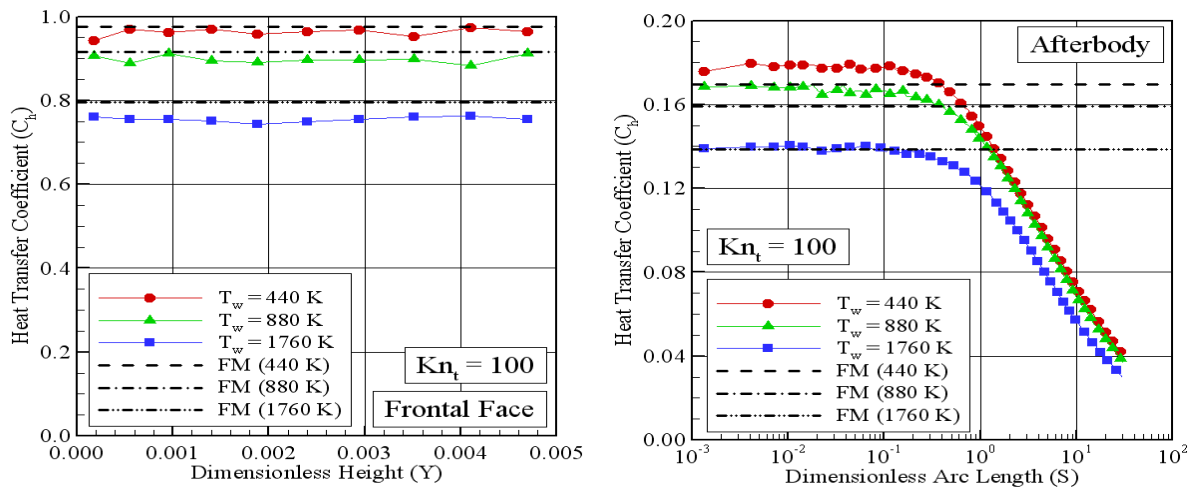


Figure 4: Heat transfer coefficient C_h along the (a) frontal face and the (b) afterbody surface as a function of the wall temperature for leading edge corresponding to Knudsen number Kn_t of 100.

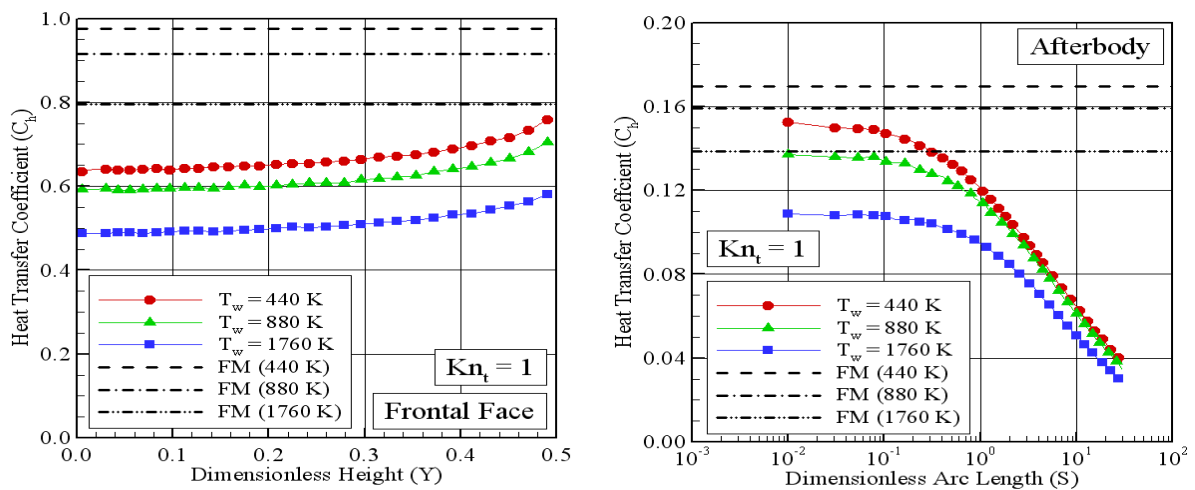


Figure 5: Heat transfer coefficient C_h along the (a) frontal face and the (b) afterbody surface as a function of the wall temperature for leading edge corresponding to Knudsen number Kn_t of 1.

6.3. Pressure Coefficient

The pressure coefficient C_p is defined as being,

$$C_p = \frac{p_w - p_\infty}{\frac{1}{2} \rho_\infty V_\infty^2} \quad (3)$$

where p_w is the pressure acting on the body surface and p_∞ is the freestream pressure.

The pressure p_w on the body surface is calculated by the sum of the normal momentum fluxes of both incident and reflected molecules at each time step as follows,

$$p_w = p_i + p_r = \sum_{j=1}^N \{ [m_j v_{\eta j}]_i + [m_j v_{\eta j}]_r \} \quad (4)$$

where v_η is the normal velocity component of the molecules (see Fig. (1b)).

The effect on pressure coefficient C_p due to variations on the leading edge thickness and on the wall temperature is demonstrated in Figs. 6 and 7. Figure 6 displays the pressure coefficient C_p along the body surface for the $Kn_t = 100$ ($t/\lambda_\infty = 0.01$) case, and Fig. 7 for the $Kn_t = 1$ ($t/\lambda_\infty = 1$) case, the bluntest case investigated. The results for pressure coefficient as well as for the other surface quantities corresponding to the $Kn_t = 10$ ($t/\lambda_\infty = 0.1$) case have been leaved out because they are intermediate to the other cases shown. Plotted along with the computational solutions for pressure coefficient is the pressure coefficient limit predicted by the free molecular flow. It is found from the free molecular flow equations values for C_p along the frontal-face surface of 2.25, 2.35 and 2.50 for wall temperature of 440 K, 880 K and 1760 K, respectively. As expected, the pressure coefficient along the frontal-face surface for the $Kn_t = 100$ case approaches the free molecular limit, as shown in Fig. 6(a).

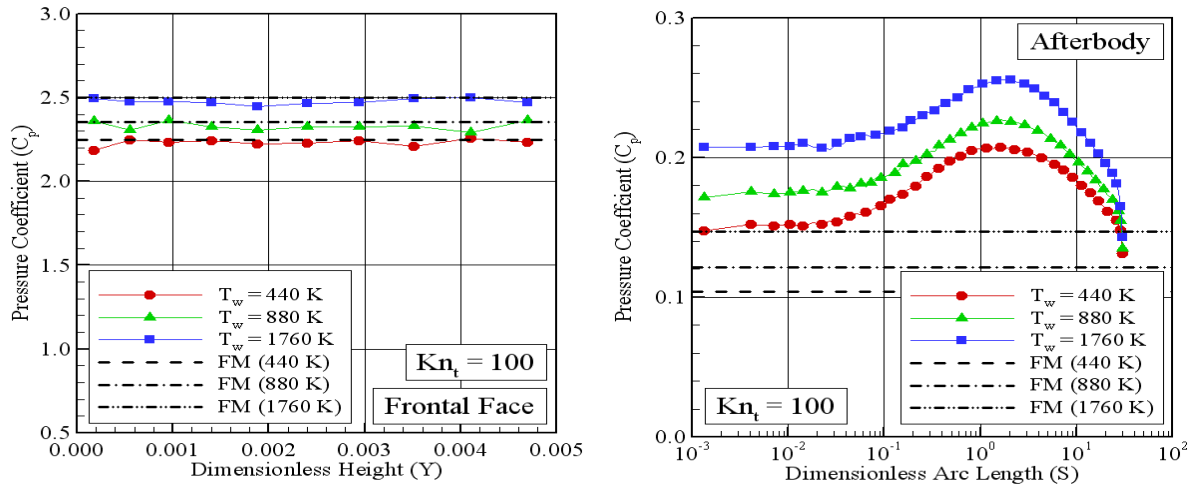


Figure 6: Pressure coefficient C_p along the (a) frontal face and the (b) afterbody surface as a function of the wall temperature for leading edge corresponding to Knudsen number Kn_t of 100.

Referring to Fig. 6, it is found that the wall temperature rise investigated has no expressive effect on the pressure coefficient for the bluntest leading edge, $Kn_t = 1$, whereas it increases slightly the pressure coefficient on the frontal-face surface for the sharpest case

investigated, $Kn_t = 100$. At this point, it is important to recognize from the number flux distribution in Figs. 3 and 4 that significant changes in the number flux occur due to variations not only on the leading edge thickness but also on the wall temperature.

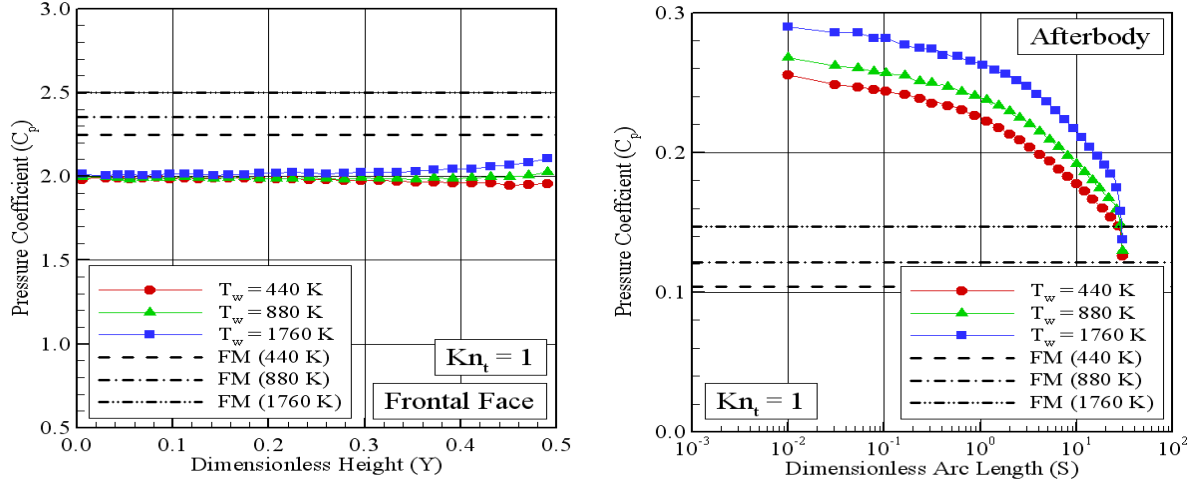


Figure 7: Pressure coefficient C_p along the (a) frontal face and the (b) afterbody surface as a function of the wall temperature for leading edge corresponding to Knudsen number Kn_t of 1.

For the $Kn_t = 1$ case, it is apparent (not shown) from the contributions of incident and reflected components of the wall pressure (see Eq. (4)) that the energetic scattered molecules play a more significant role, since the incident component of the pressure coefficient decreases and the reflected one increases with increasing the wall temperature. Hence, the insensitivity of the pressure coefficient to wall temperature variations in the range investigated, shown in Fig. 7(a), is primarily attributed to a counterbalance between the number flux reduction and the normal momentum rise related to the reflected molecules.

6.4. Skin Friction Coefficient

The skin friction coefficient C_f is defined as being,

$$C_f = \frac{\tau_w}{\frac{1}{2}\rho_\infty V_\infty^2} \quad (5)$$

where τ_w is the shear stress acting on the body surface.

The shear stress τ_w on the body surface is calculated by averaging the tangential momentum transfer of the molecules impinging on the surface. For the diffuse reflection model imposed for the gas-surface interaction, reflected molecules have a tangential moment equal to zero, since the molecules essentially lose, on average, their tangential velocity component. In this context, the tangential momentum flux of the incident molecules is defined as follows,

$$\tau_w = \sum_{j=1}^N m_j v_{\xi j} \quad (6)$$

where v_{ξ} is the tangential velocity component of the molecules.

The variation of skin friction coefficient C_f with wall temperature and with leading-edge thickness is depicted in Figs. 8 and 9 for Kn_t of 100 and 1, respectively. At the frontal-face surface, it is noted that the skin friction coefficient is zero along the surface for the sharpest leading edge investigated, Fig. 8(a). In contrast, for the bluntest leading edge, Fig. 9(a), the skin friction coefficient C_f increases at the vicinity of the frontal-face/afterbody junction of the leading edge. At the afterbody surface, the skin friction coefficient presents basically a similar tendency for sharp or blunt leading edges.

Of particular interest in this set of plots is the effect of wall temperature rise on the skin friction coefficient. It is found that the skin friction coefficient is not sensitive to wall temperature variation, provided that the gas-surface interaction is diffuse, as was assumed in this simulation. The overall shear stress τ_w is zero for fully specular reflection and is entirely due to the incident molecules for fully diffuse reflection.

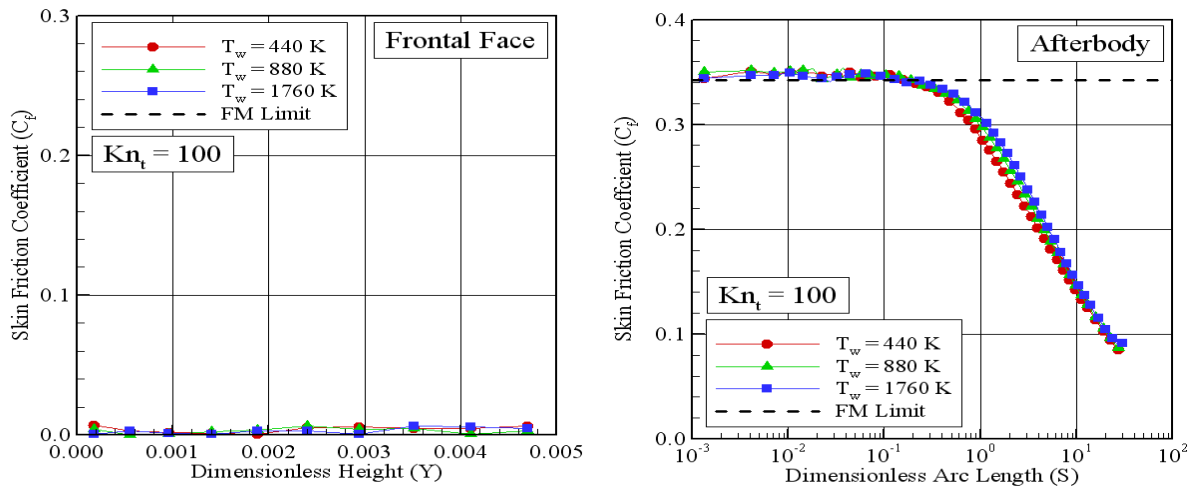


Figure 8: Skin friction coefficient C_f along the (a) frontal face and the (b) afterbody surface as a function of the wall temperature for leading edge corresponding to Knudsen number Kn_t of 100.

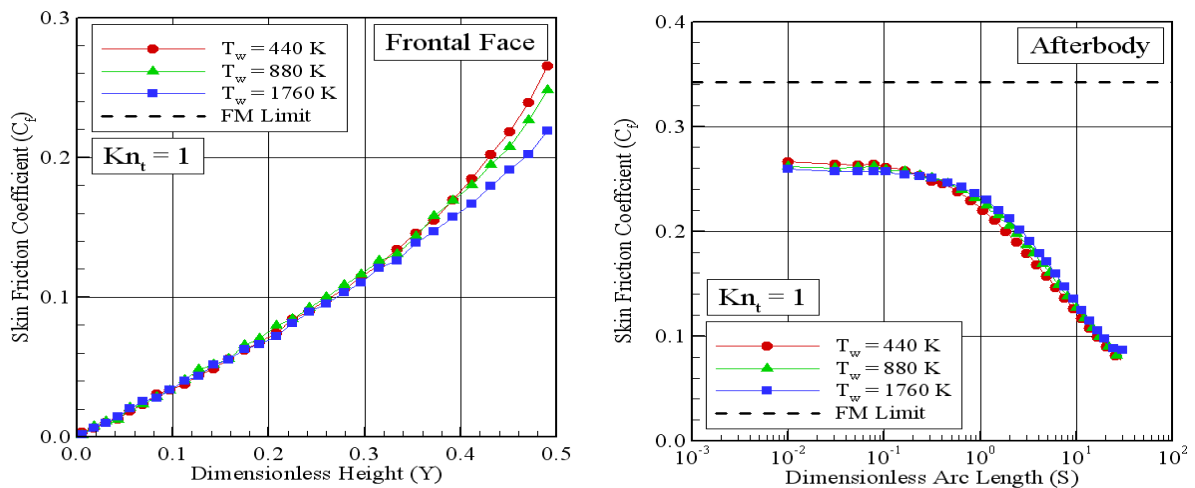


Figure 9: Skin friction coefficient C_f along the (a) frontal face and the (b) afterbody surface as a function of the wall temperature for leading edge corresponding to Knudsen number Kn_t of 1.

6.5. Total Drag Coefficient

The total drag coefficient C_d is defined as being,

$$C_d = \frac{F}{\frac{1}{2} \rho_\infty V_\infty^2 H} \quad (7)$$

where F is the resultant force acting on the body surface and H is the height at the matching point common to the leading edges (see Fig. 1(a)).

The drag force is obtained by the integration of the pressure p_w and shear stress τ_w distributions along the body surface, from the stagnation point to the station L (see Fig. 1(a)), which corresponds to the tangent point common to all of the body shapes. It is important to mention that the values for the total drag presented in this section were obtained by assuming the shapes acting as leading edges. Consequently, no base pressure effects were taken into account on the calculations.

Changes in the total drag coefficient C_d due to variations on the wall temperature and on the leading-edge thickness are displayed in Fig. 10 for Knudsen number Kn_t of 100, 10 and 1. In this set of figures, the contributions of the pressure C_{pd} and skin friction drag C_{fd} to the total drag coefficient are also illustrated. For comparison purpose, the total drag coefficient for the case investigated is tabulated in Table 3. It is apparent from these set of diagrams that as the leading edge becomes blunter, i.e., the frontal-face thickness increases, the contribution of the pressure drag to the total drag increases and the contribution of the skin friction drag decreases, and the net effect results in a slightly increase in the total drag. It is also seen that the total drag increases slightly with increasing the wall temperature.

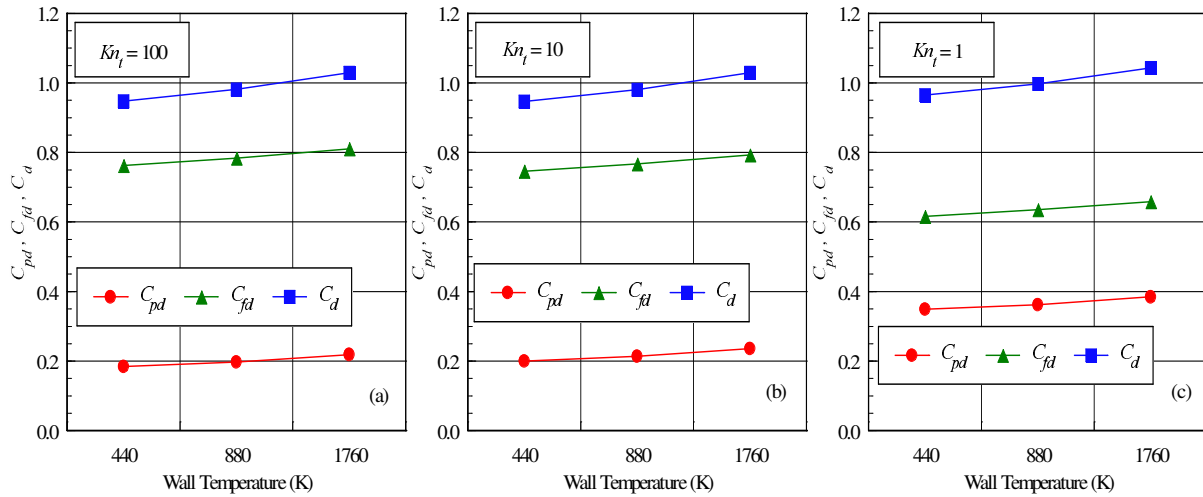


Figure 10: Pressure drag C_{pd} , skin friction drag C_{fd} and total drag coefficient C_d as a function of the wall temperature for leading edge thickness corresponding to Knudsen number Kn_t of (a) 100 and (b) 10 and (c) 1.

Table 3: Total drag coefficient C_d for the leading edges.

T_w	$Kn_t = 100$	$Kn_t = 10$	$Kn_t = 1$
440 K	0.947	0.947	0.965
880 K	0.981	0.981	0.997
1760 K	1.029	1.029	1.043

7. CONCLUDING REMARKS

Computations of a rarefied hypersonic flow on sharp and blunt leading edges have been performed by using the Direct Simulation Monte Carlo method. The calculations provided information concerning the nature of the aerodynamic surface quantities acting on the frontal face and on the afterbody surface for a family of truncated wedges.

Effects of body surface temperature on the wall heat flux, wall pressure, wall shear stress, and total drag for a wide range of parameters were investigated. The wall temperature varied from 440 K to 1760 K, set to be from 2 to 8 times the freestream temperature. In addition to that, the leading-edge thickness ranged from 0.01 to 1 of the freestream mean free path, corresponding to thickness Knudsen numbers from 100 to 1. Cases considered in this study covered the hypersonic flow from the transitional flow regime to the free molecular flow regime.

It was found that changes on the frontal-face thickness as well as on the wall temperature affected the aerodynamic surface quantities in different ways. As expected, the analysis showed that the heat flux to the body surface decreased not only with the wall temperature rise but also with increasing the frontal-face thickness, since the leading edge became blunter.

It was also found that the total drag slightly increased with increasing the frontal-face thickness as well as the wall temperature.

It is important to emphasize that this investigation has taken into account for a representative number of effects. Nevertheless, a number of improvements to a realistic leading edge design is still desirable. The DSMC method has been used to assess the aerodynamic surface quantities on truncated wedges by considering constant wall temperature. In a realistic design, temperature not only changes along the body surface but also inside the leading edge. In this scenario, a more detailed analysis that includes the conjugate heat transfer problem seems to be a challenge.

REFERENCES

- Alexander, F. J., Garcia, A. L., & Alder, B. J., 1998, Cell size dependence of transport coefficient in stochastic particle algorithms. *Physics of Fluids*, vol. 10, n. 6, pp. 1540-1542.
- Alexander, F. J., Garcia, A. L., & Alder, B. J., 2000, Erratum: Cell size dependence of transport coefficient in stochastic particle algorithms. *Physics of Fluids*, vol. 12, n. 3, pp. 731-731.
- Bird, G. A., 1981, Monte Carlo simulation in an engineering context. In Sam S. Fisher, ed., *Progress in Astronautics and Aeronautics: Rarefied gas Dynamics*, vol. 74, part I, pp. 239-255, AIAA, New York.
- Bird, G. A., 1989, Perception of numerical method in rarefied gasdynamics. In E. P. Muntz, and D. P. Weaver and D. H. Campbell, eds., *Rarefied gas Dynamics: Theoretical and Computational Techniques*, vol. 118, pp. 374-395, Progress in Astronautics and Aeronautics, AIAA, New York.
- Bird, G. A., 1994, *Molecular Gas Dynamics and the Direct Simulation of Gas Flows*. Oxford University Press, Oxford, England, UK.
- Borgnakke, C. & Larsen, P. S., 1975, Statistical collision model for Monte Carlo simulation of polyatomic gas mixture. *Journal of computational Physics*, vol. 18, n. 4, pp. 405-420.

- Garcia, A. L. & Wagner, W., 2000, Time step truncation error in direct simulation Monte Carlo. *Physics of Fluids*, vol. 12, n. 10, pp. 2621-2633.
- Guo, K. & Liaw, G.-S., 2001, A review: boundary conditions for the DSMC method. In *Proceedings of the 35th AIAA Thermophysics Conference*, AIAA Paper 2001-2953, Anaheim, CA.
- Hadjiconstantinou, N. G., 2000, Analysis of discretization in the direct simulation Monte Carlo. *Physics of Fluids*, vol. 12, n. 10, pp. 2634-2638.
- Nonweiler, T. R. F., 1959, Aerodynamic problems of manned space vehicles. *Journal of the Royal Aeronautical Society*, vol. 63, Sept, pp. 521-528.
- Santos, W. F. N., 2002, Truncated leading edge effects on flowfield structure of a wedge in low density hypersonic flight speed. In *9th Brazilian Congress of Thermal Engineering and Sciences (ENCIT 2002)*, Caxambu, MG, Brazil.
- Santos, W. F. N., 2003, Compressibility effects on flowfield structure of truncated leading edge in low density hypersonic flow. In *17th International Congress of Mechanical Engineering (COBEM 2003)*, São Paulo, SP, Brazil.
- Santos, W. F. N., 2004, The effect of incomplete surface accommodation on heat transfer and drag of truncated wedge in rarefied regime. In *3rd Brazilian Congress of Mechanical Engineering (CONEM 2004)*, Belém, PA, Brazil.
- Santos, W. F. N., 2005, Flat-faced leading-edge effects in low-density hypersonic wedge flow. *Journal of Spacecraft and Rockets*, vol. 42, n. 1, pp. 22-29.
- Santos, W. F. N., 2006, Effects of compressibility on aerodynamic surface quantities over low-density hypersonic wedge flow. *Journal of the Society of Mechanical Sciences and Engineering*, vol. 28, n. 3, pp. 362-372.
- Santos, W. F. N., 2008, Surface temperature impact on the upstream disturbance of truncated wedge in hypersonic non-equilibrium flow. In *VIII Symposium of Computational Mechanics (SIMMEC 2008)*, Belo Horizonte, MG, Brazil.